nature communications

Article

https://doi.org/10.1038/s41467-023-38411-x

Ligand-induced activation and G protein coupling of prostaglandin $F_{2\alpha}$ receptor

Received: 23 November 2022

Accepted: 2 May 2023

Published online: 09 May 2023

Check for updates

Canrong Wu[1,7] ✉, Youwei Xu[1,7], Qian He[1], Dianrong Li[2], Jia Duan[1], Changyao Li[3,4], Chongzhao You[1], Han Chen[5], Weiliang Fan[2], Yi Jiang[3,4] & H. Eric Xu[1,6] ✉

Prostaglandin $F_{2\alpha}$ ($PGF_{2\alpha}$), an endogenous arachidonic acid metabolite, regulates diverse physiological functions in many tissues and cell types through binding and activation of a G-protein-coupled receptor (GPCR), the $PGF_{2\alpha}$ receptor (FP), which also is the primary therapeutic target for glaucoma and several other diseases. Here, we report cryo-electron microscopy (cryo-EM) structures of the human FP bound to endogenous ligand $PGF_{2\alpha}$ and anti-glaucoma drugs LTPA and TFPA at global resolutions of 2.67 Å, 2.78 Å, and 3.14 Å. These structures reveal distinct features of FP within the lipid receptor family in terms of ligand binding selectivity, its receptor activation, and G protein coupling mechanisms, including activation in the absence of canonical PIF and ERY motifs and G_q coupling through direct interactions with receptor transmembrane helix 1 and intracellular loop 1. Together with mutagenesis and functional studies, our structures reveal mechanisms of ligand recognition, receptor activation, and G protein coupling by FP, which could facilitate rational design of FP-targeting drugs.

Prostanoids are a class of oxygenated arachidonic acid metabolites that include prostaglandin $F_{2\alpha}$ ($PGF_{2\alpha}$), prostaglandin D_2 (PGD_2), prostaglandin E_2 (PGE_2), thromboxane A_2 (TXA_2), and prostacyclin (PGI_2). They provoke diverse biological actions in many tissues and cell types through direct interactions with nine lipid G-protein-coupled receptors (GPCRs), prostaglandin $F_{2\alpha}$ receptor (FP), prostaglandin D_2 receptors (DP1-2), prostaglandin E_2 receptors (EP1-4), thromboxane receptor (TP) and prostacyclin receptor (IP1)[1], which comprise a subfamily of class A GPCRs. FP is encoded in humans by the PTGFR gene[2]. Stimulated by $PGF_{2\alpha}$, FP plays a pivotal role in regulating inflammation, allergic responses, intraocular pressure, and blood pressure, making it a valuable target for therapeutic discovery and development[1,3–5]. FP is highly expressed in uterine myometrium, eye, smooth muscle, skin, and ovarian[6,7]. Upon agonist stimulation, FP is predominantly coupled to the G_q subtype of G proteins, which activation leads to subsequent PKC activation and a transient calcium signaling in response to the formation of inositol triphosphate[8,9]. In addition to G_q, FP activation also induces activation of small G protein Rho via G_{12}/G_{13}[10] and activation of Raf/MEK/MAP kinase pathway through Gi[11].

Given the diverse functions of FP, it has been targeted for therapeutic development. $PGF_{2\alpha}$, the endogenous FP activator, entered a clinical trial for glaucoma treatment[12]. However, its clinical application was limited by intolerable side effects, possibly caused by its low selectivity for FP receptor[12]. Since then, selective FP agonists have attracted extensive attention and have been developed for the treatment of glaucoma[5], scalp alopecia[13], and vitiligo[14]. From 1996 to 2012, several FP-selective prostaglandin analogs (PGAs) were approved by the United States Food and Drug Administration (FDA) for glaucoma treatment. As a prodrug of a selective FP receptor agonist, latanoprost (LTP) was approved to treat glaucoma for the first time in 1996. It has

[1]State Key Laboratory of Drug Research, Shanghai Institute of Materia Medica, Chinese Academy of Sciences, Shanghai 201203, China. [2]Sironax (Beijing) Co., Ltd., Beijing 102206, China. [3]Lingang Laboratory, Shanghai 200031, China. [4]School of Life Science and Technology, ShanghaiTech University, 201210 Shanghai, China. [5]Department of Biochemistry and Molecular Biology, School of Basic Medical Sciences, Fujian Medical University, Fuzhou, Fujian 350108, China. [6]University of Chinese Academy of Sciences, Beijing 100049, China. [7]These authors contributed equally: Canrong Wu, Youwei Xu.
✉e-mail: wucanrong@simm.ac.cn; eric.xu@simm.ac.cn

also been used to treat scalp alopecia[15] and vitiligo[14] in recent years. Latanoprost acid (LTPA), 17-phenyl-13,14-dihydro $PGF_{2\alpha}$, is an active metabolic form of LTP. Another fluorinated PGA prodrug, tafluprost (TFP), was first approved for the treatment of glaucoma in 2012[16]. Tafluprost acid (TFPA), 15-deoxy-15,15-difluoro-16-phenoxy $PGF_{2\alpha}$, is the active metabolic form of TFP. Due to their high efficacy, these PGAs have been the first-line drug in clinics for the treatment of glaucoma. However, through post-marketing surveillance, 5–20% of patients suffered side effects such as conjunctival congestion and headache, including intolerance responses toward these PGAs[17–19]. Improving the selectivity of these drugs to the FP receptor and elucidating the molecular mechanisms underlying the functional selectivity of individual prostanoid receptor family members are highly important and clinically relevant.

Extensive efforts have been made to clarify how the binding of endogenous and synthetic ligands with various pharmacological profiles regulate FP's downstream signaling[8–11]. However, the molecular details defining the binding modes of ligands remain largely unknown, which is partly attributed to the scarcity of the structural information on ligands bound FP complex. Understanding the mechanism of prostaglandin-FP signaling and identifying differences in the ligand selectivity of prostaglandin receptors may assist in the development of selective drugs with improved safety.

Here we present three cryo-EM structures of G protein-coupled FP in complex with its endogenous ligand $PGF_{2\alpha}$ and with two synthetic agonists, LTPA and TFPA, at global resolutions of 2.67, 2.78, and 3.14 Å. Combined with functional characterizations of mutated receptors, these structures reveal conserved and divergent mechanisms of ligand binding, receptor activation, and G protein coupling by FP.

Results

Cryo-EM analysis and overall structure

To facilitate the expression of FP complexes, we introduced a BRIL tag to the N-terminus of the wild-type (WT) receptor[20,21]. A $G\alpha_q$ chimera was engineered based on the mini-$G\alpha_s$ scaffold with an N-terminal replacement of corresponding sequences of $G\alpha_{i1}$ to facilitate the binding of scFv16[22–24]. Hereinafter, $G\alpha_q$ reference to $G\alpha_q$ chimera. The FP-G_q complex was further stabilized by the NanoBiT strategy[25]. Incubation of $PGF_{2\alpha}$/LTPA/TFPA with membranes from cells co-expressing receptors and heterotrimer G_q proteins in the presence of scFv16 and Nb35 enables efficient assembly of the $PGF_{2\alpha}$/LTPA/TFPA -FP-G_q complexes, which produces highly homogenous complex samples for structural studies[26] (Supplementary Figs. 1–3, Table 1). The structures of the FP-G_q-scFv16-Nb35 complexes with $PGF_{2\alpha}$, LTPA, and TFPA were determined by cryo-EM to the resolutions of 2.67, 2.78, and 3.14 Å (Fig. 1a, Supplementary Figs. 1–4). The high-quality density map allowed unambiguous model building for the receptor structure containing residues 29–323, except for two invisible residues in the intracellular loop 3 (ICL3) (residues 238 and 239). The density maps are also clear for three agonists, most residues of the G_q heterotrimer, scFv16, and Nb35 (Fig. 1b, c Supplementary Fig. 4).

The overall structure of the active FP receptor is highly similar to those of active EP2 (PDB code: 7CX2) and EP4 (PDB code: 7D7M), with root mean square deviation (RMSD) values of 1.27 and 1.23 Å, respectively. FP folds into a canonical seven-transmembrane helical domain (TMD). All three extracellular loops (ECLs 1–3) were well defined, where ECL2 forms a β-hairpin loop, which is stabilized by the highly conserved disulfide bond between $C186^{ECL2}$ and $C108^{3.25}$. The β-hairpin ECL2 of FP resembles those of EP2 and EP4, and tightly caps the extracellular region (Fig. 1d). We superpose the TMD structures of $PGF_{2\alpha}$-bound FP with PGE_2-bound EP2 and EP4 to compare their overall receptor conformations and ligand-binding pockets. A notable structural difference occurs in the H8 of these receptors. The H8 of FP is almost perpendicular to that of EP2, with a rotation of 82.3°, and is closer to the cell membrane compared with the H8 of EP4. (Fig. 1e). In addition, although these ligands share a similar chemical scaffold and relatively conserved binding pocket in these three receptors, $PGF_{2\alpha}$ displays a distinct binding pose from PGE_2 in these complexes (Fig. 1e), as detailed below.

The $PGF_{2\alpha}$ binding pocket of FP

The endogenous ligand $PGF_{2\alpha}$ is mainly composed of three parts, a carboxyl group-containing α-chain, a five-membered ring (F ring) with two hydroxyl groups, and a hydrophobic ω chain with one hydroxyl group at ω6 position (Fig. 2a). The cryo-EM map enabled the unambiguous assignment of $PGF_{2\alpha}$ within the receptor pocket. $PGF_{2\alpha}$ is well resolved in the FP ligand-binding pocket by adopting an L-shape conformation with its carboxyl group-containing α-chain fitting into a hydrophilic sub-pocket near the top of the receptor (Fig. 2a), formed by residues from TM1, TM7, and ECL2 (Fig. 2b). The carboxyl group in the α-chain of $PGF_{2\alpha}$ forms a salt bridge with $R291^{7.40}$ and hydrogen bonds with $T184^{EL2}$ and $Y92^{2.65}$. Mutations of residues $R291^{7.40}$, $T184^{EL2}$, and $Y92^{2.65}$, which are highly conserved in prostanoid receptors and participate directly in receptor binding, lead to decreased activity of $PGF_{2\alpha}$ (Fig. 2b–d, Supplementary Fig. 5-6). Although electrostatic contacts are the major driving force for the interactions between the α-chain and the positively charged binding pocket of FP, several hydrophobic residues also play important roles. Particularly, we did see the side chain of $M115^{3.23}$ forms lone pair-π interaction with ethylene linkage in the α-chain (Fig. 2b, c, Supplementary Fig. 6). Mutating this methionine in FP to alanine decreased the affinity for $PGF_{2\alpha}$ by approximately 100-fold (Fig. 2d, Supplementary Fig. 5). The F ring is located in a sub-pocket formed by TM1, TM2, and TM7 (Fig. 2b). These two hydroxyl groups in F ring mainly participate in polar interactions with the receptor. Particularly, these hydroxyl groups form hydrogen bonds with $S33^{1.39}$ and $T294^{7.43}$, which are not conserved among prostanoid receptor family members, indicating that this part mainly contributes to the selectivity of $PGF_{2\alpha}$ to FP. Meanwhile, mutation of $S33^{1.39}$ or $T294^{7.43}$ in FP to alanine significantly impaired the affinity to $PGF_{2\alpha}$ (Fig. 2d, Supplementary Fig. 5). Besides α chain and F ring, the ω chain penetrates into the hydrophobic pocket formed by TM5, TM6, and TM7. This alkyl chain forms hydrophobic interactions with $F205^{5.41}$, $W262^{6.48}$, $F265^{6.51}$, and $L290^{7.39}$. Mutations of these residues in FP to alanine significantly impaired the affinity to $PGF_{2\alpha}$ (Fig. 2d, Supplementary Fig. 5). Besides hydrophobic interaction, the ω6 hydroxy group forms a hydrogen bond with $H81^{2.54}$, which mutated to alanine also caused a dramatically reduced the activity of $PGF_{2\alpha}$ to FP by over 1000 folds (Fig. 2d, Supplementary Fig. 5). Collectively, the α-chain and ω-chain that bind to the sub-pockets with highly conserved residues, mainly contributes to high receptor binding affinity, while the F ring could be important for receptor selectivity.

Specific engagement of LTPA and TFPA with FP

Even though FP is an important therapeutic target for many diseases, the poor selectivity of $PGF_{2\alpha}$ has hampered its clinical application. LTPA and TFPA, two synthetic relative selective FP agonists, have been widely used in clinical treatment for diseases including glaucoma. LTPA showed high affinity to FP with an EC_{50} of 3.6 nM but only moderate potency to EP1 and EP3, with an EC_{50} of 6.9 and 17 μM, respectively[27]. Compared to $PGF_{2\alpha}$, the selectivity was enhanced by more than 100 times[27]. TFPA is the most potent FP agonist (EC_{50}: 0.4 nM) and has a fairly low potency to the other members of the prostanoid receptor family except for EP3 (EC_{50}: 67 nM)[28]. LTPA, TFPA, and $PGF_{2\alpha}$ all have shared α-chain and F ring, while LTPA and TFPA have bulky substitutions in the ω-chain compared to $PGF_{2\alpha}$ (Fig. 3 a-e). LTPA and TFPA bond to FP in nearly identical binding poses as $PGF_{2\alpha}$ did, displaying a similar "L"-shape configuration in these two solved structures (Fig. 3a). Likewise, the carboxylate groups of LTPA and TFPA form strong polar interactions with $R291^{7.40}$, $T184^{EL2}$, and $Y92^{2.65}$, the

https://doi.org/10.1038/s41467-023-38411-x

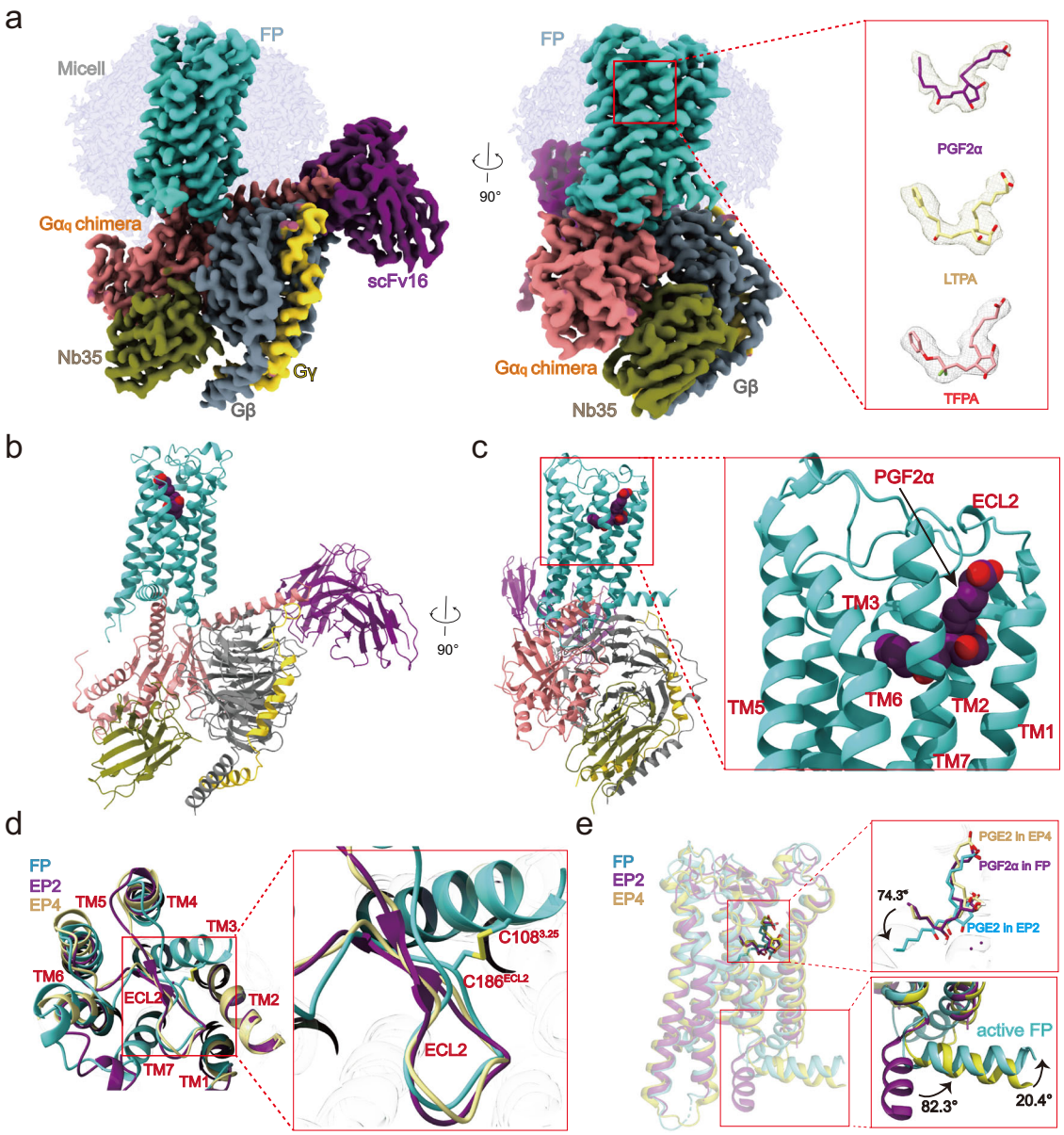

Fig. 1 | Cryo-EM structures of FP–G_q complexes. a Cryo-EM density of FP-G_q in complex with $PGF_{2\alpha}$, LTPA, or TFPA. FP in Medium Turquoise, $G\alpha_q$ in light Coral, Gβ in slate gray, Gγ in gold, ScFv16 in dark magenta, Nb35 in Olive, $PGF_{2\alpha}$ in purple, LTPA in yellow, and TFPA in light coral. **b**, **c** Cartoon representation of the $PGF_{2\alpha}$-FP-G_q complex. FP in Green, $G\alpha_q$ in brown, Gβ in slate gray, Gγ in gold, ScFv16 in dark magenta, Nb35 in Olive, and $PGF_{2\alpha}$ in purple. **d**, **e** Comparison of the FP–G_q complex with the EP2–Gs complex (PDB ID: 7CX2) and the EP4–Gs structure (PDB ID: 7D7M). FP shows a conserved conformation of ECL2 (green) with the other two receptors. The orientation of H8 of FP is different from the Gs-coupled receptor EP2 and EP3, and the ligand binding pose $PGF_{2\alpha}$ to FP is different from PGE_2 to EP2.

ethylene linkage in the α-chain forms a lone pair-π[29] interaction with M115$^{3.23}$, and the two hydroxy groups in the F ring form hydrogen bonds with S33$^{1.39}$ and T294$^{7.43}$ (Fig. 3b, c). Consistent with this observation, mutations of these residues in FP to alanine significantly decreased the potency of LTPA and TFPA to FP.

The derivatized ω-chain in LTPA also directly binds to FP. The phenyl group in the ω-chain of LTPA packs against F205$^{5.41}$, F265$^{6.51}$, F187^{ECL2}, L290$^{7.39}$, and W262$^{6.48}$ with hydrophobic interactions. These residues are highly conserved in FP, EP1, and EP3. Interestingly, besides forming a hydrogen bond with H81$^{2.54}$, the hydroxyl group in the ω chain forms an additional hydrogen bond with S118$^{3.35}$, which only exists in FP (Fig. 3d–f), indicating that this residue is of vital importance for the selectivity of LTPA to FP. Consistent with this finding, mutation of this serine to alanine or asparagine significantly reduced the potency of LTPA to induce FP activation (Fig. 3g, Supplementary Fig. 5).

Similar to LTPA, the phenyl group in the ω-chain of TFPA forms extensive hydrophobic interactions with FP. Moreover, the oxygen atom forms a hydron bond with the side chain of Q297, and the two fluoride groups in the carbon 12-position of TFPA form three hydrogen bonds with several residues in FP[30], which may explain its high potency to FP. One fluoride group in TFPA forms hydrogen bonds to H81$^{2.54}$ and S118$^{3.35}$, as the hydroxyl group in LTPA did. Notably, the other fluoride group forms a hydrogen bond with N84$^{2.57}$(Fig. 3e, Supplementary Fig. 6). This residue is highly diverse among prostanoid receptor family members. Intriguingly, among the other 8 prostanoid receptors, only EP3 and TP harbor a similar polar uncharged residue, threonine (Fig. 3f). Through structural analysis, mutation of N84$^{2.57}$ to threonine in FP could still form a hydrogen bond with the fluoride group (Supplementary Fig. 6). This explains its strong affinity for EP3. Consistent with this prediction, mutation of this residue to threonine does not significantly reduce ligand binding of TFPA, but mutating to alanine

https://doi.org/10.1038/s41467-023-38411-x

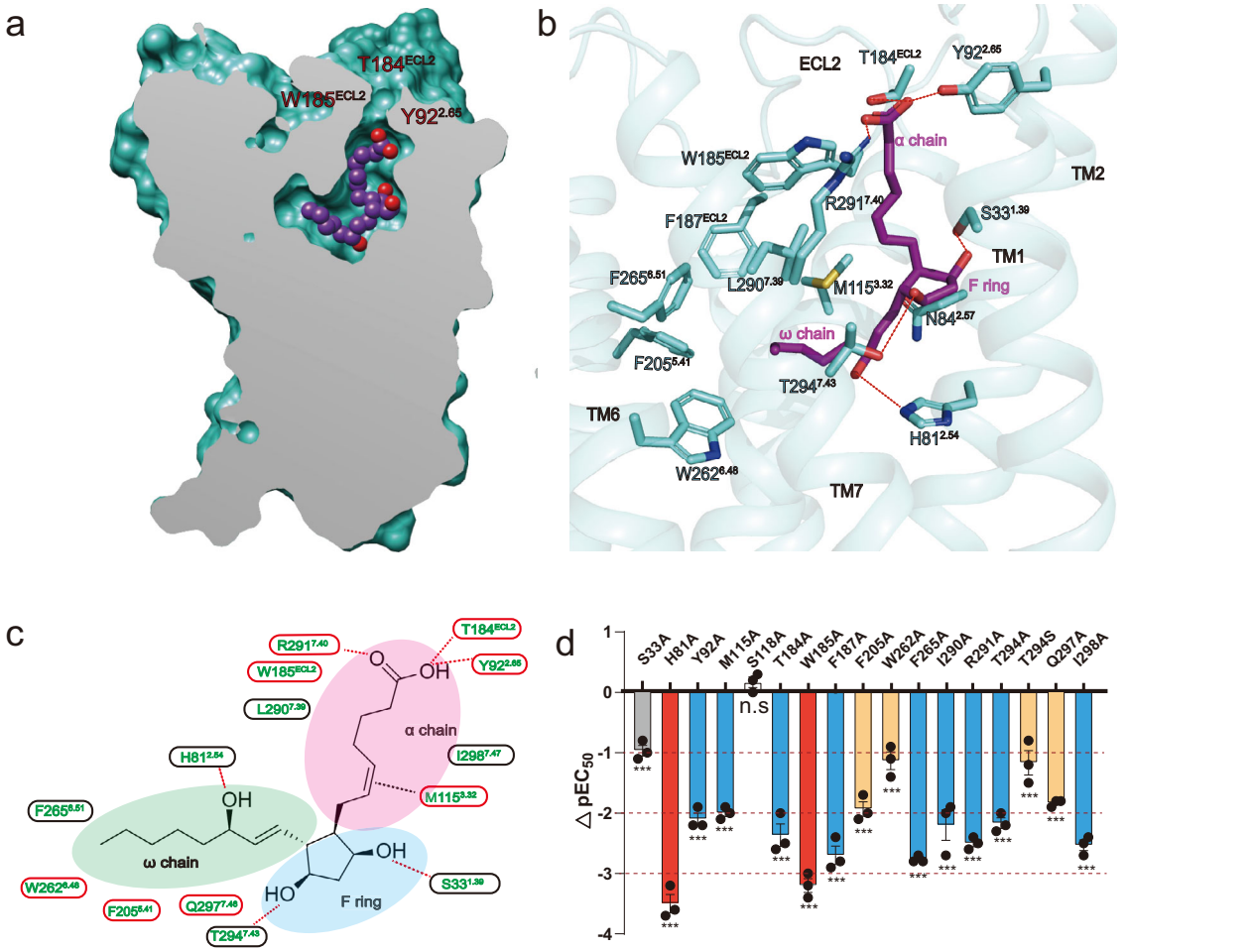

Fig. 2 | The $PGF_{2\alpha}$ binding pocket of FP. a Vertical cross-section of the $PGF_{2\alpha}$-binding pocket in FP. **b** Corresponding interactions that contribute to $PGF_{2\alpha}$ binding in FP. The hydrogen bond is depicted as a red dashed line. **c** Schematic representation of the interactions between FP and $PGF_{2\alpha}$ in 2D format and region division in FP–$PGF_{2\alpha}$ binding pockets corresponding to the structure of PGF2α (F ring, ω chain, and α chain). **d** IP1 accumulation assay of key mutants in FP that bind to $PGF_{2\alpha}$ (ΔpEC_{50} = pEC_{50} of $PGF_{2\alpha}$ to specific Mutant-pEC_{50} of $PGF_{2\alpha}$ to WT, Yellow column means $\Delta pEC_{50} \le -1$, Blue column means $\Delta pEC_{50} \le -2$, Red column means $\Delta pEC_{50} \le -3$). Data are presented as mean values ± SEM; $n = 3$ independent samples; significance was determined with a two-sided unpaired *t*-test; n.s. no significant; $^{*}p < 0.05$; $^{**}p < 0.01$; $^{***}p < 0.001$. Exact *p* values and Source data are provided as a Source Data file.

does (Fig. 3g, Supplementary Fig. 5). This hydrogen bond formed between $T^{2.57}$ in EP3 and TFPA may contribute to the high affinity of TFPA toward EP3[28].

The active structure of FP

Structural comparison of the $PGF_{2\alpha}$-bound FP-G_q complexes with the antagonist-bound TP (PDB: 6IIU)[31] supports the notion that FP in these structures is in the active state, featured by the outward displacement of the cytoplasmic end of TM6, the hallmark of class A GPCR activation, and concurrently inward shift of TM7. In addition, TM5 of FP laterally shifts relative to that of antagonist-bound TP. These conformation changes largely resemble that of the G_q-coupled 5-HT_{2A}R complex (PDB: 6WHA)[22] (Fig. 4a), but the outward amplitude of TM6 of FP is smaller than that of 5-HT_{2A}R (Fig. 4a).

Structure comparison of the active FP in complex with $PGF_{2\alpha}$ and the inactive TP bound to an antagonist provide clues for understanding the activation mechanism of FP. Upon $PGF_{2\alpha}$ binding, the ω-chain of $PGF_{2\alpha}$ approaches the toggle switch residue $W262^{6.48}$ to trigger the downward displacement of $W262^{6.48}$ by 2.4 Å (Fig. 4b, c). The movement of $W262^{6.48}$ further constitutes a hydrophobic LLW core triad, which is comprised of $L123^{3.40}$, $L213^{5.49}$, and $W262^{6.48}$, to fasten TM3, TM5, and TM6. The importance of the LLW core triad is functionally supported by the decreased potency of $PGF_{2\alpha}$ to activate $L123^{3.40}$A and $L213^{5.49}$A FP mutants (Fig. 4c, Supplementary Fig. 7). Notably, the canonical $P^{5.50}$ $I^{3.40}$ $F^{6.44}$ motif in majority of class A GPCRs[26,32] is replaced by $G214^{5.50}$ $L123^{3.40}$ $S258^{6.44}$. In our structure of active FP, $G214^{5.50}$ is sterically apart from $S258^{6.44}$ and $L123^{3.40}$, leading to the lack of the conserved PIF hydrophobic triad, thus indicating that FP employs an activation mechanism not mediated by the traditional PIF motif (Fig. 4b).

The receptor activation also accompanies the arrangement of ionic lock (D/$E^{3.49}$ $R^{3.50}$ $Y^{3.51}$, $E132^{3.49}$ $R133^{3.50}$ $C134^{3.51}$ in FP), leading to the broken of the salt bridge between $E132^{3.49}$ and $R133^{3.50}$ and the stretching of the $R133^{3.50}$ side chain towards TM6 and the latter's outward displacement of 6.7 Å compared with that of inactive TP (measured at Cα of residue 6.30). $C134^{3.51}$ in the ERC motif moves inwards, forming interactions with $I222^{5.58}$ and $T223^{5.59}$ in TM5. The importance of motif in FP activation is evidenced by the decreased $PGF_{2\alpha}$ activity on FP mutants of $E132^{3.49}$, $R133^{3.50}$, and $C134^{3.51}$ (Supplementary Fig. 7). Intriguingly, unlike its cognate residue $R312^{8.47}$ in TP, the side chain of $R308^{8.47}$ in FP undergoes a large-scale upward rotation and forms a hydrogen bond with $Q250^{6.36}$, which leads to the inward shift of the cytoplasmic end of TM7 and the upshift of H8 (Fig. 4d). The importance of this hydrogen bond in FP activation is evidenced by the loss of

https://doi.org/10.1038/s41467-023-38411-x

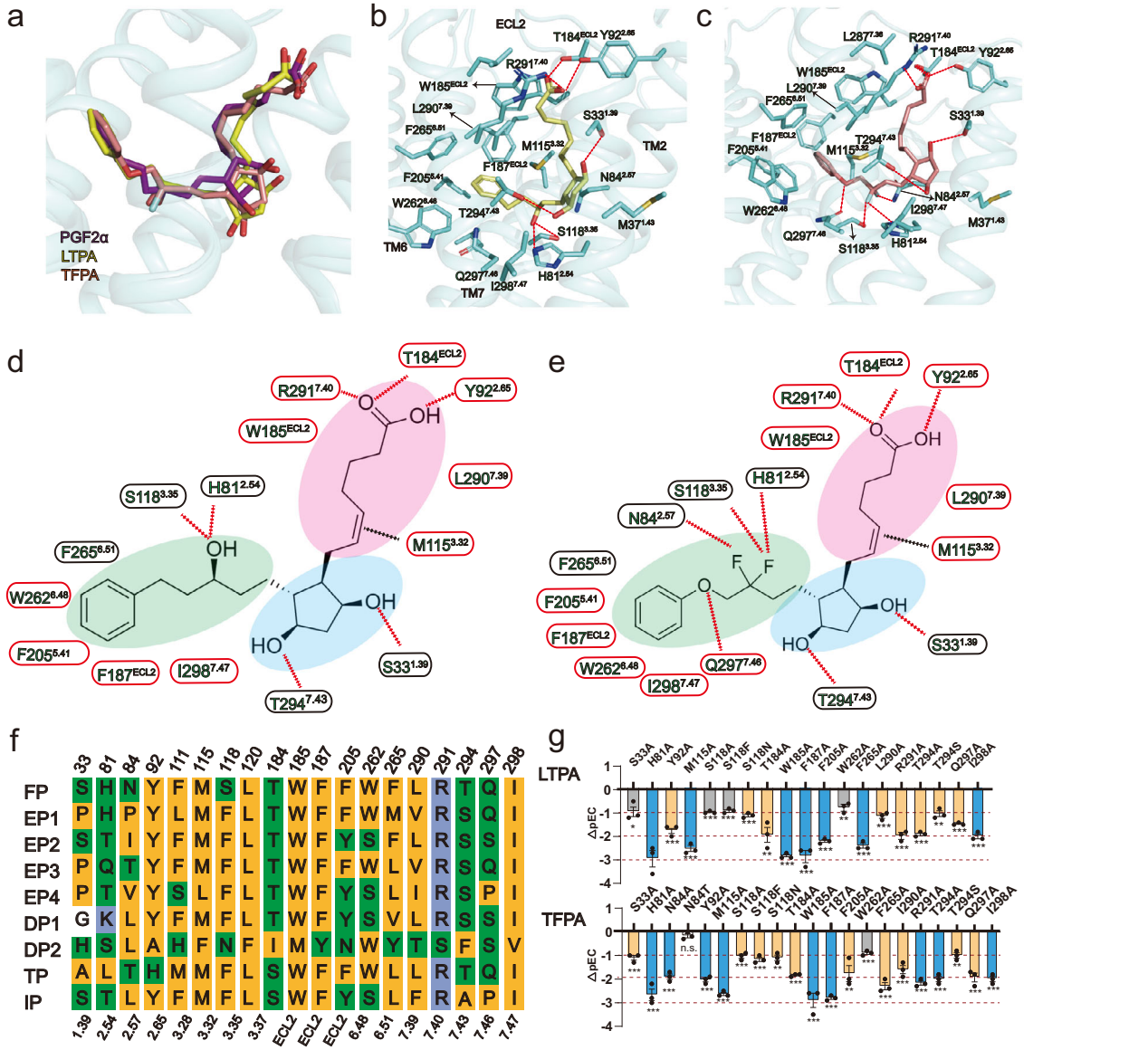

Fig. 3 | Specific engagement of LTPA and TFPA with FP. a Superimposition of the $PGF_{2\alpha}$ bound FP with LTPA bound FP and TFPA bound FP aligned at the ligand binding pocket. **b**, **c** Detail interactions of LTPA-FP and TFPA-FP were shown. H-bonds were depicted as red dashed lines. **d**, **e** 2D representation of contacts in LTPA-FP and TFPA-FP. The polar bonds were presented by red dotted lines. Conserved residues that formed interactions with ligands are presented in a red oval frame. **f** Sequence alignment of prostanoid receptors. Hydrophobic residues are in yellow, polar charged residues in blue, and polar uncharged residues in green. g, IP1 accumulation assay of key mutants in FP that bind to LTPA or TFPA (ΔpEC_{50} = pEC_{50} of agonists to specific Mutant FP-pEC_{50} of $PGF_{2\alpha}$ to WT FP, Yellow column means $\Delta pEC_{50} \leq -1$, Blue column means $\Delta pEC_{50} \leq -2$). Data are presented as mean values ± SEM; $n = 3$ independent samples; significance was determined with two-side unpaired *t*-test; n.s. no significant; $^{*}p < 0.05$; $^{**}p < 0.01$; $^{***}p < 0.001$. Exact *p* values and Source data are provided as a Source Data file.

$PGF_{2\alpha}$ activity on FP mutants of $R133^{3.50}A$, $Q250^{6.36}A$, and $R308^{8.47}A$. (Supplementary Fig. 7) Noteworthily, the arginine at position 8.47 is highly conserved across prostaglandin receptors, while $Q^{6.36}$ only exists in several class A receptors, including EP1, EP3, and FP, indicating that this interaction network could also exist in active structures of EP1 and EP3.

FP-G_q coupling

The notable outward displacement of TM6 at the cytoplasmic side opens a cavity to accommodate the $G\alpha_q$ subunit. Structural comparisons of FP-G_q with G_q-coupled CCK_AR and $5HT_{2A}R$ reveal a difference in the conformations of TM1, TM6, and $G\alpha_q$ subunits among these G_q-coupled GPCR complexes (Fig. 5a). The cytoplasmic end of FP TM1 and TM6 undergoes a remarkably inward displacement relative to CCK_AR and $5HT_{2A}R$. Consequently, the C-terminus of the α5 helix of the $G\alpha_q$ subunit in the FP-G_q complex rotates toward TM7 and H8 to avoid clashes with TM6 and forms extra hydrophobic interactions with side chains of residues in H8, accompanied by the rotation of the entire $G\alpha_q$ subunit (Fig. 5a). This alteration triggers a 14° tilt of the αN helix of $G\alpha_q$, bringing it closer to the cytoplasmic end of TM4 in the FP-G_q complex relative to CCK_AR-G_q and $5HT_{2A}R$-G_q complexes (Fig. 5a). In addition to coupling G_q by interactions with H8 and TM4, the engagement of G_q is also maintained by interactions with FP from TM1, TM2, TM3, TM5, TM4, TM6, ICL1, and ICL2. The side chain of $E132^{3.49}$ of the $E^{3.49}$ (D) $R^{3.50}C^{3.51}$ (Y) motif in TM3 makes a direct hydrogen bond interaction with the side chain of the Y356 of α5 (Fig. 5b, c).

Like other G_q-coupled GPCR[33], the ICL2 of FP facilitates broad interactions with G_q to stabilize the complex. Typically, ICL2 adopts a helix conformation and inserts into the groove formed by the αN, β2–β3 loop, and α5 helix of $G\alpha_q$. Interestingly, we identified several distinct interactions between TM6 and $G\alpha_q$. For instance, the $H244^{6.30}$ forms a hydrogen bond interaction with the side chain of Q350 of $G\alpha_q$,

https://doi.org/10.1038/s41467-023-38411-x

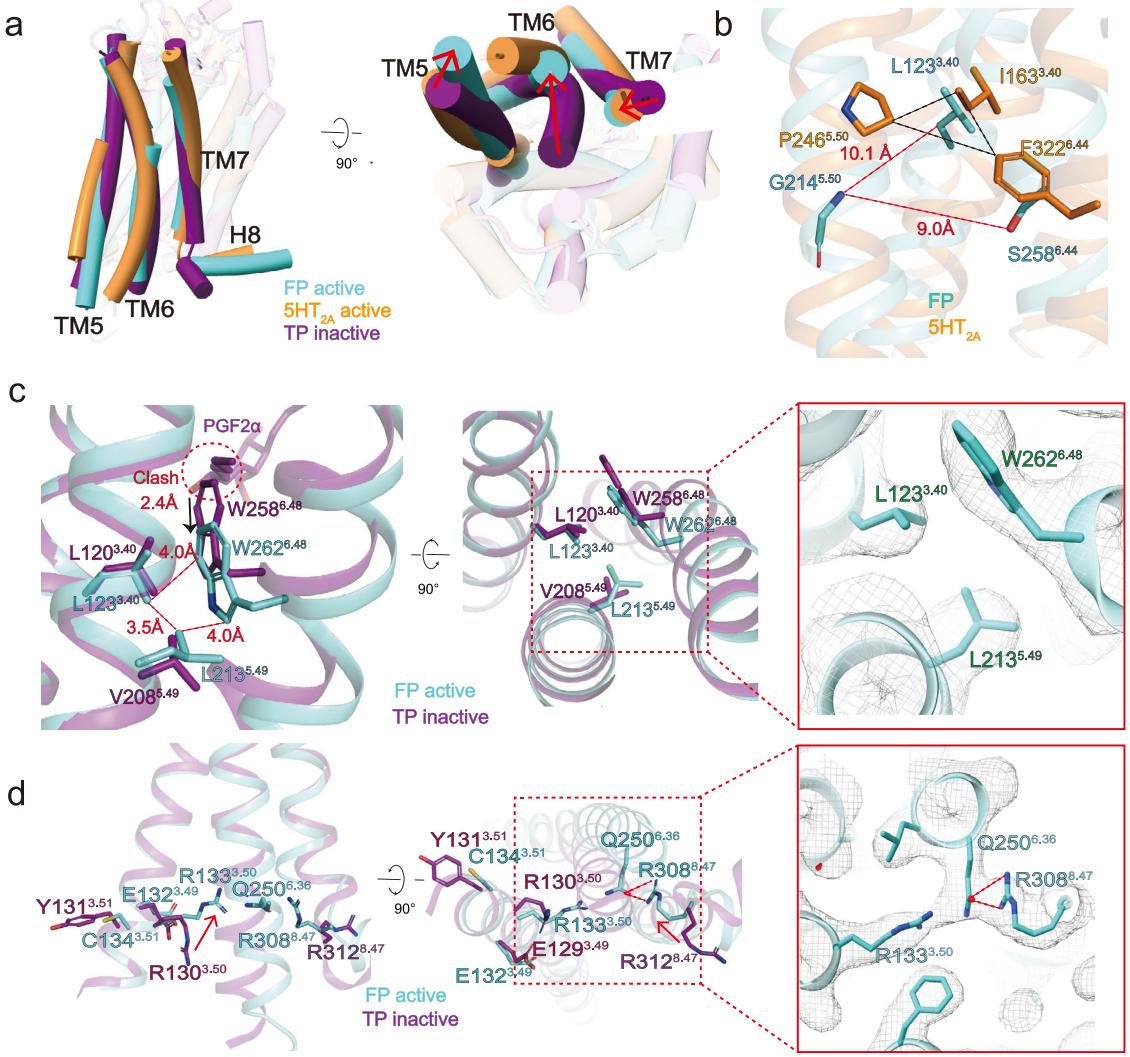

Fig. 4 | The active structure of the FP. a Superimposition of G_q-coupled FP with the G_q-coupled 5-HT_{2A}R complex and antagonist-bound TP (PDB: 6IIU). FP in Green, 5-HT_{2A}R in brown, and TP in purple. **b** Superimposition of G_q-coupled FP with G_q-coupled 5-HT_{2A} aligned at the PIF motif. **c** Superimposition of G_q-coupled FP with antagonist-bound TP aligned at the LLW motif. The left panel is a magnified view of the LLW motif. The right panel is the top view of the LLW motif. Residues are shown in the sticks, with the correspondent cryo-EM density represented in the mesh. **d** Superimposition of G_q-coupled FP with antagonist-bound TP aligned at the D(E)RY(C) motif and RQR motif. The left panel is a magnified view of the D(E)RY(C) motif and RQR motif. The right panel is the top view of D(E)RY(C) and RQR motifs. Residues are shown in the sticks, with the correspondent cryo-EM density represented in the mesh.

and E246$^{6.32}$ forms a hydrogen bond interaction with the side chain of N357 of $G\alpha_q$ (Fig. 5d). Mutating of H244$^{6.30}$ and E246$^{6.32}$ to alanine destabilizes the complex and reduces the IP1 accumulation of FP (Fig. 5d, Supplementary Fig. 6). Most notably, unlike other solved G_q-coupled GPCR structures, the extensive interactions of TM1, ICL1, and TM2 of FP with G_q play an important role in stabilizing the complex (Fig. 5e). F58 packs against L358 and V359 of $G\alpha_q$ stabilized by hydrophobic interaction, and K63 packs against R37 of $G\alpha_q$. S62 forms a hydrogen bond with E355 of $G\alpha_q$ (Fig. 5e). Mutating S62 to alanine almost abolished the IP1 accumulation of FP (Fig. 5e, Supplementary Fig. 7), supporting that the direct interactions of TM1, ICL1, and TM2 with G protein are important for FP to couple with G protein.

Discussion

Glaucoma is the leading cause of permanent eyesight loss in the world[34]. According to the World Health Organization (WHO), 79.6 million individuals suffered from glaucoma in 2020, and the number of patients may increase to 111.8 million by 2040[35]. Activation of prostaglandin receptors like FP, EP1–EP4, and DP showed anti-glaucoma effects. Research for the discovery of pharmaceutical drugs selectively targeting each of these receptors has been extensively conducted, whereas only FP selective agonists are approved for treatment due to their minimal side-effect profile[36]. Elucidating the mechanism underlying the functional selectivity of individual FP receptors is of utmost importance for developing new drugs with higher selectivity towards individual prostaglandin receptors to avoid or reduce undesirable side effects.

In this study, we present the cryo-EM structures of FP-G_q in complex with its endogenous ligand $PGF_{2\alpha}$ as well as two synthetic agonists LTPA and TFPA. Through structure analysis of the $PGF_{2\alpha}$–FP–G_q complex, the carboxylate-containing α-chain that binds to the sub-pocket with highly conserved residues contributes to the majority of the high potency of the receptor. In contrast, the F ring is important for receptor selectivity. Similar to PGE_2 to EP3, the hydrophobic ω-chain directly interacts with the toggle switch W262$^{6.48}$ in FP and forms hydrophobic interactions with a set of hydrophobic residues. The hydroxyl group in the ω-chain of LTPA forms an additional hydrogen bond with S118$^{3.35}$ in FP in the LTPA-FP-G_q structure, which may be the key to LTPA's higher selectivity to FP. Despite $PGF_{2\alpha}$ containing the hydroxyl group at the same position as LTPA that the presence of the aromatic ring and lack of carbon-to-carbon double bonds in the ω-chain of LTPA may affect the geometry of the ligand,

https://doi.org/10.1038/s41467-023-38411-x

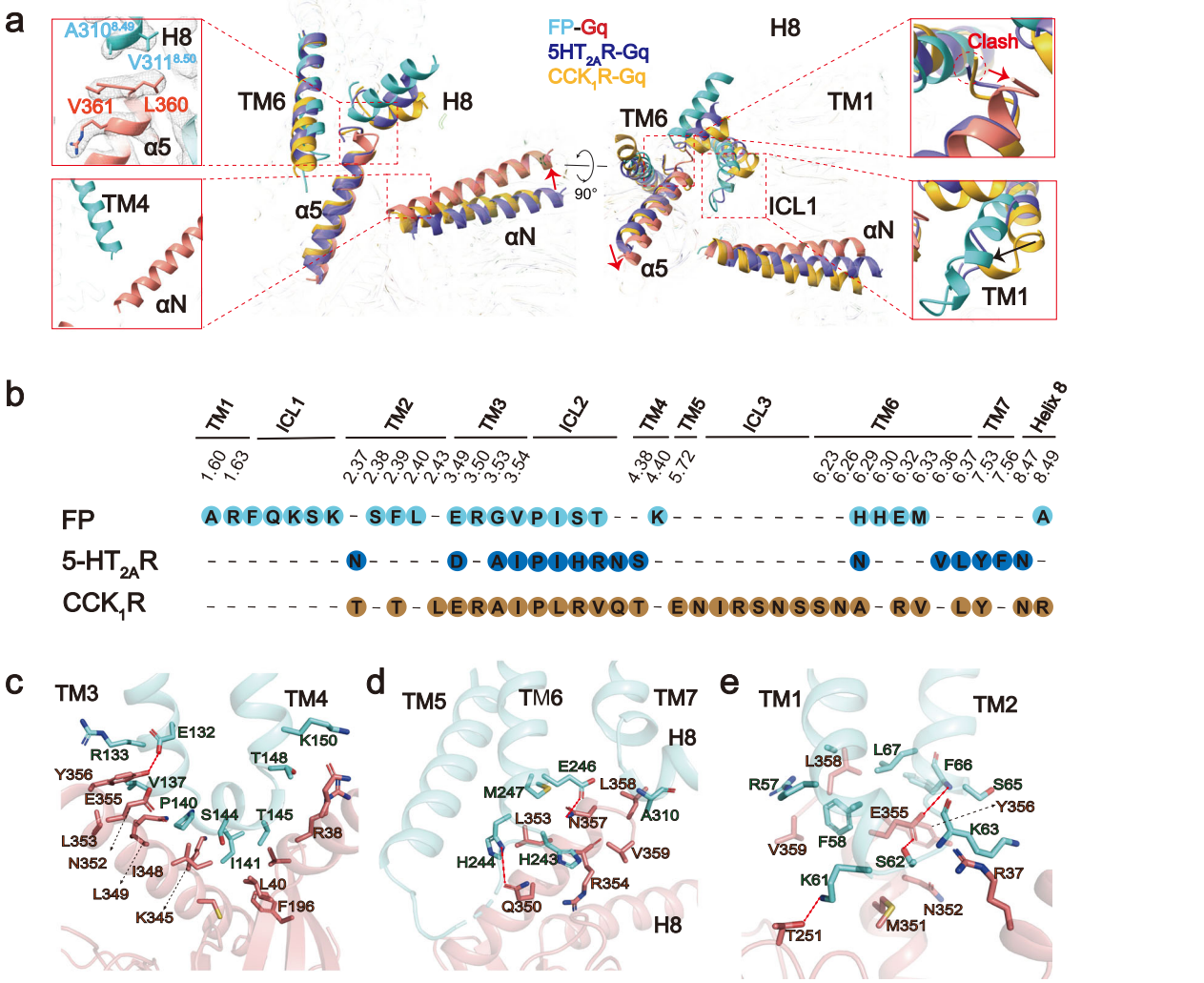

Fig. 5 | FP–G_q coupling. a The structures of G_q-coupled FP, 5-HT_{2A}R (PDB ID: 6WHY), and CCK_1R (PDB ID: 7MBY) complexes were superimposed based on TM2, TM3 and TM4, FP is shown in light sea green, 5-HT_{2A}R in blue and CCK_1R in yellow. This panel is shown with views an orthogonal view (left) and a cytoplasmic view (right); the red arrows indicate the tilt of the α5 helix of $G\alpha_q$ from the FP–G_q complex compared to the 5-HT_{2A}R–G_q or CCK_{A1}–G_q complexes. **b** the residues in FP, 5-HT_{2A}R, and CCK_{A1} that contact G_q. **c**–**e** The detailed interactions of ICL2 with $G\alpha_q$ (**c**), TM6 with the α5 helix of $G\alpha_q$ (**d**) and TM1, TM2, and ICL1 with the αN and α5 helices of $G\alpha_q$ (**e**). The hydrogen bonds are depicted as dashed lines.

indicating that these modifications in the ω-chain of PGAs may improve their selectivity to FP. Compared with the LTPA, TFPA forms an extra hydrogen bond to $N84^{2.57}$ in FP with a fluoride group in the ω chain. EP3 harbors a similar polar uncharged residue, $T^{2.57}$, which may form a hydrogen bond with the fluoride group of TFPA. Although TFPA had a higher affinity for FP than LTPA, its selectivity needs to be further improved. These structures revealed the ligand recognition of FP, which will serve as templates for the rational design of a new generation of potent agonists with desired selectivity profiles.

Through structural comparison and mutagenesis studies, we also elucidated the mechanisms of receptor activation and G protein coupling by FP. FP has neither the traditional 'PIF' core triad nor the DRY motif that is commonly involved in the activation of class A GPCRs, instead FP senses ligand binding by the conserved toggle switch $W^{6.48}$ to tether TM3–TM5–TM6 through a hereby identified LLW core triad consisting of $L123^{3.40}$, $L213^{5.49}$. Intriguingly, mutation of the $W262^{6.48}$ in FP to alanine did not entirely abolish these three agonists induced activation of FP. It is speculated that the ω chain of $PGF_{2\alpha}$, LTPA, or TFPA in W262A mutant still induces the activation of mutated FP because it may point downward in a similar manner to EP2 (Fig. 1e), which naturally lacks $W^{6.48}$ at the toggle switch residue position[37]. In the FP receptor, the conserved D/ERY motif is replaced by ERC, which only exists in several class A GPCRs, like EP1, IP, and Neurotensin receptor type 2. Interestingly, in the active FP structure, $Q250^{6.36}$ induces an upswing of the side chain of $R308^{8.47}$ and forms a hydrogen bond with it that leads to the inward shift of the cytoplasmic end of TM7 and the upshift of H8. $R^{8.47}$ is particularly conserved in prostaglandin receptors but rarely exists in other class A GPCRs, and $Q^{6.36}$ only exists in several class A receptors, including EP1, EP3, and FP. All these key residues for activation in FP are harbored by EP1, which also primarily couples with G_q. Thus, this activation mechanism should be applicable to both FP and EP1, which have the same unique residues.

The distinct features of the active FP structures also define the way of G_q protein coupling. Specifically, the TM1, ICL1, and TM2 of FP form extensive interactions with G_q, which, to our knowledge, haven't been shown in any other reported G_q-coupled GPCR structures. These observed characteristics in the FP-G_q complex structures, including the arrangement of the 7TM bundle, the ligand-binding mode, the ligand-induced receptor activation, and the manner of G protein coupling, expand the understanding of lipid recognition and GPCR-G_q coupling mechanism. Collectively, our results reveal conserved and diverse mechanisms of ligand binding, receptor activation, and G protein coupling by FP.

Methods

Constructs

The full-length human FP was modified to contain the N-terminal thermally stabilized BRIL[20] to enhance receptor expression and the addition of an N-terminal Flag tag. LgBiT was inserted at the C-terminus of the human FP using homologous recombination. The modified FP was cloned into the pFastBac (Thermo Fisher Scientific) vectors using the ClonExpress II One Step Cloning Kit (Vazyme Biotech). An engineered $G\alpha_q$ chimera was generated based on the mini-Gαs scaffold with its aa1-18 replaced by corresponding sequences of $G\alpha_{i1}$, aa348-359 replaced by corresponding sequences of $G\alpha_q$, A33, H35, A87, V92, D107, V115, R137, N144, C151, F155, K158, V161, K163, D171, and D319 replaced by corresponding residues in $G\alpha_q$, designated as $mG\alpha_{s/q/iN}$. Human wild-type (WT) Gβ1, human Gγ2, and a single-chain antibody scFv16[38], as well as a Gβ1 fused with SmBiT at its C-terminus, were cloned into pFastBac vectors.

Insect cell expression

Human FP, G_q chimera, Gβ1, Gγ, and scFv16 were co-expressed in High Five insect cells (Invitrogen) using the baculovirus method (Expression Systems). Cell cultures were grown in ESF 921serum-free medium (Expression Systems) to a density of 2–3 million cells per mL and then infected with six separate baculoviruses at a suitable ratio. The culture was collected by centrifugation 48 h after infection, and cell pellets were stored at −80 °C.

Complex purification

Cell pellets were thawed in 20 mM HEPES pH 7.4, 150 mM NaCl, 10 mM $MgCl_2$, and $CaCl_2$ supplemented with Protease Inhibitor Cocktail (TargetMol). For the $PGF_{2\alpha}$/LTPA/TFPA-FP-G_q-scFv16 complexes, 10 μM $PGF_{2\alpha}$/LTPA/TFPA (MedChemExpress) and 2 mg Nb35 were added. The suspension was incubated for 1 h at room temperature, and the complex was solubilized from the membrane using 0.5% (w/v) lauryl maltose neopentyl glycol (LMNG) (Anatrace) and 0.1% (w/v) cholesteryl hemisuccinate (CHS) (Anatrace) for 2 h at 4 °C. Insoluble material was removed by centrifugation at 70,000*g* for 35 min, and the supernatant was immobilized on the Flag resin (SinoBiological). The resin was then packed and washed with 30 column volumes of 20 mM HEPES pH 7.4, 150 mM NaCl, 0.01% (w/v) LMNG, 0.002% CHS, and 10 μM ligand. The complex sample was eluted in buffer containing 20 mM HEPES pH 7.4, 150 mM NaCl, 0.01% (w/v) LMNG, 0.002% CHS, 10 μM ligand, and 0.2 mg/ml FLAG peptide (GenScript). Complex fractions were concentrated with a 100-kDa molecular weight cut-off (MWCO) Millipore concentrator for further purification. The complex was then subjected to size-exclusion chromatography on a Superdex 6 Increase 10/300 GL column (GE Healthcare) pre-equilibrated with size buffer containing 20 mM HEPES pH 7.4,150 mM NaCl, 0.00075% (w/v) LMNG, 0.00025% (w/v) GDN (Anatrace), 0.00025% digitonin (w/v), 0.00015% CHS, and10 μM ligand to separate complexes. Eluted fractions were evaluated by SDS-PAGE, and those consisting of receptor-G_q protein complexes were pooled and concentrated for cryo-EM experiments.

Cryo-EM data collection

Cryo-EM grids were prepared with the Vitrobot Mark IV plunger (FEI) set to 4 °C and 100% humidity. Three microliters of the sample were applied to the glow-discharged gold R1.2/1.3 holey carbon grids. The sample was incubated for 10 s on the grids before blotting for 3 s (double-sided, blot force −2) and flash-frozen in liquid ethane immediately. For FP–G_q–$PGF_{2\alpha}$ complex, FP-G_q-LTPA complex, and FP-G_q-TFPA complex datasets, 3902, 7972, and 6513 movies were collected, respectively, on a Titan Krios equipped with a Gatan K3 direct electron detection device at 300 kV with a magnification of 105,000, corresponding to a pixel size 0.824 Å. Image acquisition was performed with EPU Software (FEI Eindhoven, Netherlands). We collected a total of 36 frames accumulating to a total dose of 50 e^- $Å^{-2}$ over 2.5 s exposure.

Cryo-EM image processing

MotionCor2 was used to perform the frame-based motion-correction algorithm to generate a drift-corrected micrograph for further processing, and CTFFIND4 provided the estimation of the contrast transfer function (CTF) parameters[39,40]. All subsequent steps, including particle picking and extraction, two-dimensional (2D) classification, three-dimensional (3D) classification, 3D refinement, CTF refinement, Bayesian polishing, post-processing, and local resolution estimation, were performed using Relion3.0[41].

For FP–G_q–$PGF_{2\alpha}$ complex dataset, 115 aligned micrographs were deleted because of contaminations or bad ice quality. A total of 3,391,620 particles were extracted from the cryo-EM micrographs and followed by two rounds of reference-free 2D classification, yielding 895,825 particles after clearance. Mask 3D classification on the receptor part was used to separate out 479,164 particles which resulted in a clearer density of PTGFR. We refined these particles, which led to a structure at 3.24 Å global resolution. After the postprocessing, the particles were reconstituted to a 2.67 Å structure (Supplementary Fig. 1).

For FP–G_q–LTPA complex dataset, 1438 aligned micrographs were deleted because of contaminations or bad ice quality. A total of 5,478,774 particles were extracted from the cryo-EM micrographs and followed by two rounds of reference-free 2D classification, yielding 1,181,590 particles after clearance. The global 3D classification was used to separate out 437,740 particles. We then continued the processing in Relion3.0 and refined 437,740 particles, which led to a structure at 3.40 Å global resolution. After CTF refinement, Bayesian polishing, and postprocessing, then the particles were reconstituted to a 2.78 Å structure (Supplementary Fig. 2).

For FP–G_q–TFPA complex dataset, 279 aligned micrographs were deleted because of contaminations or bad ice quality. A total of 5,774,308 particles were extracted from the cryo-EM micrographs and followed by two rounds of reference-free 2D classification, yielding 2,418,674 particles after clearance. The global 3D classification was used to separate out 805,802 particles. Two rounds of mask 3D classification on the receptor part were used to separate out 578,962 particles which resulted in a clearer density of PTGFR. We refined these particles, which led to a structure at 3.35 Å global resolution. After CTF refinement, Bayesian polishing, and postprocessing, then the particles were reconstituted to a 3.14 Å structure (Supplementary Fig. 3). We also performed postprocessing of all three final maps with DeepEMhancer[42].

Model building

A predicted FP structure from Alphafold2 was used as the starting reference model for receptor building[43]. Structures of $G_{\alpha q}$, Gβ, Gγ, and the scFv16 were derived from PDB entry 7WKD[44] and were rigid body fit into the density. All models were fitted into the EM density map using UCSF Chimera[45], followed by iterative rounds of manual adjustment and automated rebuilding in COOT[46] and PHENIX[47], respectively. The model was finalized by rebuilding in ISOLDE[48], followed by refinement in PHENIX with torsion-angle restraints to the input model. The final model statistics were validated using Comprehensive validation (cryo-EM) in PHENIX[47] and provided in Supplementary Table 1. All structural figures were prepared using Chimera[45], Chimera X[49], and PyMOL (Schrödinger, LLC.).

Inositol phosphate accumulation assay

IP-One production was measured using the IP-One HTRF kit (Cisbio)[50]. Briefly, AD293 cells (Agilent) were grown to a density of 400,000–500,000 cells per mL and then infected with separate plasmids at a suitable concentration. The culture was collected by

centrifugation 24 h after incubation at 37 °C in 5% CO_2 with a Stimulation Buffer. The cell suspension was then dispensed in a white 384-well plate at a volume of 7 µl per well before adding 7 µl of ligands. The mixture was incubated for 1 h at 37 °C. IP-One-d2 and anti-IP-One Cryptate dissolved in Lysis Buffer (3 µl each) were subsequently added and incubated for 15-30 min at room temperature before measurement. Intracellular IP-One measurement was carried out with the IP-One HTRF kit and EnVision multi-plate reader (PerkinElmer) according to the manufacturer's instructions. Data were normalized to the baseline response of the ligand. pEC_{50} E_{min}, and E_{max} for each curve were calculated by GraphPad Prism 8.0. ΔpEC_{50} equals pEC_{50} of agonists to specific Mutant minus pEC_{50} of agonists to WT. Data are presented as mean values ± SEM; $n = 3$ independent samples; n.s. no significant; $^{*}p < 0.05$; $^{**}p < 0.01$; $^{***}p < 0.001$.

Receptor surface expression

Cell-surface expression levels of WT or mutants FP were quantified by flow cytometry. AD293 cells were seeded at a density of 1.5×10^5 per well into 12-well culture plates. Cells were grown overnight and then transfected with 1.0 µg FP construct by FuGENE® HD transfection reagent in each well for 24 h. After 24 h of transfection, cells were washed once with PBS and then detached with 0.2% (w/v) EDTA in PBS. Cells were blocked with PBS containing 5% (w/v) BSA for 15 min at room temperature before incubating with primary anti-Flag antibody (diluted with PBS containing 5% BSA at a ratio of 1:300, Sigma-Aldrich, F3165) for 1 h at room temperature. Cells were then washed three times with PBS containing 1% (w/v) BSA and then incubated with anti-mouse Alexa-488-conjugated secondary antibody (diluted at a ratio of 1:1000, Thermo Fisher, A-11029) at 4 °C in the dark for 1 h. After another three times of washing, cells were collected, and fluorescence intensity was quantified in a Luminex flow cytometer system (Guava® easyCyte) through a Luminex guavaSoft 4.5 at excitation 488 nm and emission 519 nm. Approximately 10,000 cellular events per sample were collected, and data were normalized to the wild-type FP. Experiments were performed at least three times, and data were presented as means ± SEM.

Statistics

All functional study data were analyzed using GraphPad Prism 8.0 (Graphpad Software Inc.) and showed as means ± S.E.M. from at least three independent experiments in triplicate. The significance was determined with a two-sided, unpaired *t*-test, and $^{*}p < 0.05$ was considered statistically significant.

Reporting summary

Further information on research design is available in the Nature Portfolio Reporting Summary linked to this article.

Data availability

The atomic coordinates and the electron microscopy maps have been deposited in the Protein Data Bank (PDB) under accession numbers 8IUK, 8IUL, and 8IUM and Electron Microscopy Data Bank (EMDB) accession number EMD-35724, EMD-35725, and EMD-35726 for the PGF2α–FP–G_q and the LTPA–FP–G_q and the TFPA–FP–G_q complex, respectively. Previously published structures can be accessed via accession codes: 7CX2; 7D7M; 6IIU; 6WHY; 7MBY; 6WHA; 7WKD. Source data are provided in this paper.

References

1. Woodward, D. F., Jones, R. L. & Narumiya, S. International Union of Basic and Clinical Pharmacology. LXXXIII: classification of prostanoid receptors, updating 15 years of progress. *Pharm. Rev.* **63**, 471–538 (2011).
2. Duncan, A. M., Anderson, L. L., Funk, C. D., Abramovitz, M. & Adam, M. Chromosomal localization of the human prostanoid receptor gene family. *Genomics* **25**, 740–742 (1995).
3. Scher, J. U. & Pillinger, M. H. The anti-inflammatory effects of prostaglandins. *J. Investig. Med.* **57**, 703–708 (2009).
4. Zhang, J., Gong, Y. & Yu, Y. PG F(2α) receptor: a promising therapeutic target for cardiovascular disease. *Front. Pharm.* **1**, 116 (2010).
5. Ota, T., Aihara, M., Narumiya, S. & Araie, M. The effects of prostaglandin analogues on IOP in prostanoid FP-receptor-deficient mice. *Invest. Ophthalmol. Vis. Sci.* **46**, 4159–4163 (2005).
6. Mukhopadhyay, P., Bian, L., Yin, H., Bhattacherjee, P. & Paterson, C. Localization of EP(1) and FP receptors in human ocular tissues by in situ hybridization. *Invest. Ophthalmol. Vis. Sci.* **42**, 424–428 (2001).
7. Sugimoto, Y. et al. Cloning and expression of a cDNA for mouse prostaglandin F receptor. *J. Biol. Chem.* **269**, 1356–1360 (1994).
8. Abramovitz, M. et al. Cloning and expression of a cDNA for the human prostanoid FP receptor. *J. Biol. Chem.* **269**, 2632–2636 (1994).
9. Carrasco, M. P., Phaneuf, S., Asbóth, G. & López Bernal, A. Fluprostenol activates phospholipase C and Ca2+ mobilization in human myometrial cells. *J. Clin. Endocrinol. Metab.* **81**, 2104–2110 (1996).
10. Pierce, K. L., Fujino, H., Srinivasan, D. & Regan, J. W. Activation of FP prostanoid receptor isoforms leads to Rho-mediated changes in cell morphology and in the cell cytoskeleton. *J. Biol. Chem.* **274**, 35944–35949 (1999).
11. Melien, Ø., Thoresen, G. H., Sandnes, D., Østby, E. & Christoffersen, T. Activation of p42/p44 mitogen-activated protein kinase by angiotensin II, vasopressin, norepinephrine, and prostaglandin F2α in hepatocytes is sustained, and like the effect of epidermal growth factor, mediated through pertussis toxin-sensitive mechanisms. *J. Cell. Physiol.* **175**, 348–358 (1998).
12. Susanna, R. Jr. & Medeiros, F. A. The pros and cons of different prostanoids in the medical management of glaucoma. *Curr. Opin. Ophthalmol.* **12**, 149–156 (2001).
13. Johnstone, M. A. & Albert, D. M. Prostaglandin-induced hair growth. *Surv. Ophthalmol.* **47**, S185–S202 (2002).
14. Nowroozpoor Dailami, K. et al. Efficacy of topical latanoprost in the treatment of eyelid vitiligo: a randomized, double-blind clinical trial study. *Dermatol. Ther.* **33**, e13175 (2020).
15. Bhat, S., Handa, S. & De, D. A randomized comparative study of the efficacy of topical latanoprost versus topical betamethasone diproprionate lotion in the treatment of localized alopecia areata. *Indian J. Dermatol. Venereol. Leprol.* **87**, 42–48 (2021).
16. Swymer, C. & Neville, M. W. Tafluprost: the first preservative-free prostaglandin to treat open-angle glaucoma and ocular hypertension. *Ann. Pharmacother.* **46**, 1506–1510 (2012).
17. Schumer, R. A., Camras, C. B. & Mandahl, A. K. Putative side effects of prostaglandin analogs. *Surv. Ophthalmol.* **47**, S219 (2002).
18. Uusitalo, H., Pillunat, L. E. & Ropo, A. Efficacy and safety of tafluprost 0.0015% versus latanoprost 0.005% eye drops in open-angle glaucoma and ocular hypertension: 24-month results of a randomized, double-masked phase III study. *Acta Ophthalmol.* **88**, 12–19 (2010).
19. Digiuni, M., Fogagnolo, P. & Rossetti, L. A review of the use of latanoprost for glaucoma since its launch. *Expert Opin. Pharmacother.* **13**, 723–745 (2012).
20. Chun, E. et al. Fusion partner toolchest for the stabilization and crystallization of G protein-coupled receptors. *Structure* **20**, 967–976 (2012).
21. Zhuang, Y. et al. Structural insights into the human D1 and D2 dopamine receptor signaling complexes. *Cell* **184**, 931–942.e918 (2021).
22. Kim, K. et al. Structure of a hallucinogen-activated Gq-coupled 5-HT(2A) serotonin receptor. *Cell* **182**, 1574–1588.e1519 (2020).

23. Wang, Y. et al. Molecular recognition of an acyl-peptide hormone and activation of ghrelin receptor. *Nat. Commun.* **12**, 5064 (2021).
24. Yin, Y. L. et al. Molecular basis for kinin selectivity and activation of the human bradykinin receptors. *Nat. Struct. Mol. Biol.* **28**, 755–761 (2021).
25. Duan, J. et al. Cryo-EM structure of an activated VIP1 receptor-G protein complex revealed by a NanoBiT tethering strategy. *Nat. Commun.* **11**, 4121 (2020).
26. Rasmussen, S. G. et al. Crystal structure of the β2 adrenergic receptor-Gs protein complex. *Nature* **477**, 549–555 (2011).
27. Stjernschantz, J., Selén, G., Astin, M. & Resul, B. Microvascular effects of selective prostaglandin analogues in the eye with special reference to latanoprost and glaucoma treatment. *Prog. Retin. Eye Res.* **19**, 459–496 (2000).
28. Takagi, Y. et al. Pharmacological characteristics of AFP-168 (tafluprost), a new prostanoid FP receptor agonist, as an ocular hypotensive drug. *Exp. Eye Res.* **78**, 767–776 (2004).
29. Jin, M. Y. et al. Engineered non-covalent π interactions as key elements for chiral recognition. *Nat. Commun.* **13**, 3276 (2022).
30. Pietruś, W., Kafel, R., Bojarski, A. J. & Kurczab, R. Hydrogen bonds with fluorine in ligand-protein complexes-the PDB analysis and energy calculations. *Molecules* **27**, 1005 (2022).
31. Fan, H. et al. Structural basis for ligand recognition of the human thromboxane A(2) receptor. *Nat. Chem. Biol.* **15**, 27–33 (2019).
32. Steyaert, J. & Kobilka, B. K. Nanobody stabilization of G protein-coupled receptor conformational states. *Curr. Opin. Struct. Biol.* **21**, 567–572 (2011).
33. Duan, J. et al. Molecular basis for allosteric agonism and G protein subtype selectivity of galanin receptors. *Nat. Commun.* **13**, 1364 (2022).
34. Jonas, J. B. et al. Glaucoma. *Lancet* **390**, 2183–2193 (2017).
35. Tham, Y. C. et al. Global prevalence of glaucoma and projections of glaucoma burden through 2040: a systematic review and meta-analysis. *Ophthalmology* **121**, 2081–2090 (2014).
36. Lindén, C. & Alm, A. Prostaglandin analogues in the treatment of glaucoma. *Drugs Aging* **14**, 387–398 (1999).
37. Qu, C. et al. Ligand recognition, unconventional activation, and G protein coupling of the prostaglandin E(2) receptor EP2 subtype. *Sci. Adv.* **7**, eabf1268 (2021).
38. Maeda, S. et al. Development of an antibody fragment that stabilizes GPCR/G-protein complexes. *Nat. Commun.* **9**, 3712 (2018).
39. Zheng, S. Q. et al. MotionCor2: anisotropic correction of beam-induced motion for improved cryo-electron microscopy. *Nat. Methods* **14**, 331–332 (2017).
40. Rohou, A. & Grigorieff, N. CTFFIND4: fast and accurate defocus estimation from electron micrographs. *J. Struct. Biol.* **192**, 216–221 (2015).
41. Zivanov, J. et al. New tools for automated high-resolution cryo-EM structure determination in RELION-3. *Elife* **7**, e42166 (2018).
42. Sanchez-Garcia, R. et al. DeepEMhancer: a deep learning solution for cryo-EM volume post-processing. *Commun. Biol.* **4**, 874 (2021).
43. Tunyasuvunakool, K. et al. Highly accurate protein structure prediction for the human proteome. *Nature* **596**, 590–596 (2021).
44. Xu, Y. et al. Structural insights into ligand binding and activation of the human thyrotropin-releasing hormone receptor. *Cell Res.* **32**, 855–857 (2022).
45. Pettersen, E. F. et al. UCSF Chimera—a visualization system for exploratory research and analysis. *J. Comput Chem.* **25**, 1605–1612 (2004).
46. Emsley, P. & Cowtan, K. Coot: model-building tools for molecular graphics. *Acta Crystallogr. D Biol. Crystallogr.* **60**, 2126–2132 (2004).
47. Adams, P. D. et al. Recent developments in the PHENIX software for automated crystallographic structure determination. *J. Synchrotron. Radiat.* **11**, 53–55 (2004).
48. Croll, T. I. ISOLDE: a physically realistic environment for model building into low-resolution electron-density maps. *Acta Crystallogr. D Struct. Biol.* **74**, 519–530 (2018).
49. Pettersen, E. F. et al. UCSF ChimeraX: Structure visualization for researchers, educators, and developers. *Protein Sci.* **30**, 70–82 (2021).
50. Garbison, K. E. et al. in *Assay Guidance Manual* (eds S. Markossian et al.) (Eli Lilly & Company and the National Center for Advancing Translational Sciences, 2004).

Acknowledgements

The cryo-EM data were collected at the Shanghai Advanced Center for Electron Microscopy, Shanghai Institute of Materia Medica, Chinese Academy of Sciences. We thank K.W., W.H., and Q.Y. for performing cryo-EM data collection. This work was partially supported by Ministry of Science and Technology (China) grants (2018YFA0507002 to H.E.X.); Shanghai Municipal Science and Technology Major Project (2019SHZDZX02 to H.E.X.); Shanghai Municipal Science and Technology Major Project (H.E.X.); CAS Strategic Priority Research Program (XDB37030103 to H.E.X.); The National Natural Science Foundation of China (32130022 to H.E.X., 82121005 to H.E.X., 32171187 to Y.J., 82121005 to Y.J.); China Postdoctoral Science Foundation Funded Project (2021M703342 to C.W.); Shanghai Post-doctoral Excellence Program (2021429 to C.W.); Key tasks of Lingang Laboratory (LG202101-01-03 to Y.X.); the National Natural Science Foundation of China (81902085 to Y.X.).

Author contributions

C.W. designed the expression constructs and purified the protein complex supervised by H.E.X. Y.X. and J.D. prepared the grids. Y.X. performed cryo-EM data processing and model building. C.W. and Q.H. constructed all the mutated plasmids, and C.W. performed functional studies supervised by H.E.X. H.E.X. and C.W. analyzed the structures. C.W. prepared the figures and initial paper. C.Y. and Y.X. contributed to the preparation of the figures. Y.X. contributed to manuscript preparation. Q.H., D.L., H.C., C.L., and C.Y. helped with experiments. H.E.X. conceived the project and initiated collaborations with W.F., All authors discussed and commented on the paper. H.E.X. and Y.J. revised the paper, and H.E.X. supervised the project. H.E.X. and C.W. wrote the paper with input from all authors.

Competing interests

H.E.X., Y.J., C.W., Y.X., Q.H., J.D., H.C., C.L., and C.Y. declare no competing interest. W.F. and D.L. are employees of Sironax (Beijing) Co., Ltd.

Additional information

Supplementary information The online version contains supplementary material available at https://doi.org/10.1038/s41467-023-38411-x.

Correspondence and requests for materials should be addressed to Canrong Wu or H. Eric Xu.

Peer review information *Nature Communications* thanks David Thal and the other anonymous reviewer(s) for their contribution to the peer review of this work. A peer review file is available.